



The role of thin NiPi film for enhancing solar water splitting performance of Ti doped hematite



Jian Wang^a, Jianying Yang^b, Zengyao Zheng^b, Tongbu Lu^{c,d,✉}, Wenhua Gao^{a,*}

^a Department of Chemistry, Shantou University, Shantou 515063, PR China

^b National Detergent and Cosmetics Products Quality Supervision and Inspection Center (Guangdong), Shantou, 515041, PR China

^c State Key Laboratory of Optoelectronic Materials and Technologies, School of Chemistry and Chemical Engineer, and Instrumentation Analysis & Research Center, Sun Yat-Sen University, Guangzhou 510275, PR China

^d Institute for New Energy Materials and Low-Carbon Technologies, School of Materials Science and Engineering, Tianjin University of Technology, Tianjin 300384, PR China

ARTICLE INFO

Article history:

Received 23 February 2017

Received in revised form 11 April 2017

Accepted 15 June 2017

Available online 21 June 2017

Keywords:

Solar water oxidation

Ti doping

PEC regulation

NiPi coating

Surface states suppression

ABSTRACT

Ti doped hematite (α -Fe₂O₃) usually shows poor photoactivity compared with pristine Fe₂O₃ at less positive potential. Herein, a thin and relatively homogeneous nickel-hydroxyl-phosphate (NiPi) film was modified on Ti doped Fe₂O₃ electrode by a new deposit-photoelectrochemical (DPEC) regulation process for promoting hole transport at low bias. The role of Ti doping and NiPi or CoPi coating was studied by photoelectrochemical and electrochemical measurements in detail, in which NiPi coating suppressed the surface states, while CoPi coating couldn't. Ti doped Fe₂O₃ possessed relatively rich oxygen vacancies after high temperature annealing. Ti doping only improved carrier density. Desirably, the performance of NiPi was comparable with CoPi. Additional test preliminarily verified that methanol was probably an more effective hole scavenger, while PO₄³⁻ adsorbed Fe₂O₃/NiPi suppressed the oxidation of low-concentration glucose, resulting into high-energy glucose waste.

© 2017 Elsevier B.V. All rights reserved.

1. Introduction

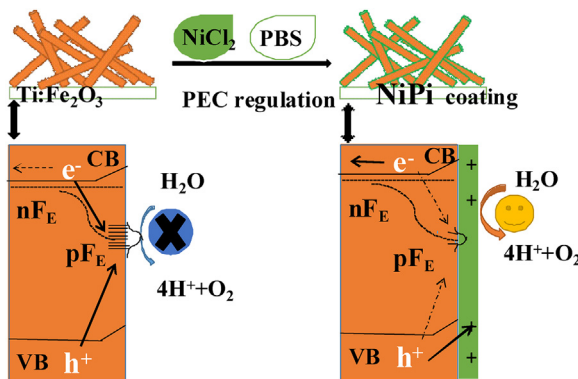
α -Fe₂O₃ is a widely studied photoanode for solar water oxidation half reaction, with many advantages including a favorable band gap of ca. 1.9–2.2 eV, suitable valence band level for water oxidation as well as earth abundance, low cost, nontoxicity, and stability in alkaline solutions [1–5]. However, the water oxidation efficiency of hematite is largely limited by (1) short lifetime of photogenerated charge carriers (<10 ps) [3,6] as well as short hole diffusion length (2~20 nm) [7–9] resulting into low bulk charge separation, (2) sluggish oxygen evolution kinetics, and (3) surface states. All resulted into poor hole injection efficiency. For the problem (1), diverse cation doping, specially, Ti⁴⁺ doping [10–14] are versatile and effective approach to enhancing the bulk charge separation efficiency of Fe₂O₃. As for the problem (2), coupling with water oxidation catalyst, i.e., IrO₂ [15,16], CoPi [2–5,17], Ni(OH)₂ [18], NiOOH [19] were usually used to accelerate the water oxidation by lower-

ing overpotential of oxygen evolution reaction (OER). A benchmark photocurrent of 3.2 mA/cm² at 1.23 V vs RHE was achieved by IrO₂-modified cauliflower-type Fe₂O₃ nanostructure electrode [16]. The photocurrent was still lower than the theoretical plateau current 12.6 mA/cm² of α -Fe₂O₃ [16], and the Fe₂O₃/IrO₂ photoanode was subjected to three adverse factors that limited its practical performance: (a) fast photocurrent decay in 200 s due to flaky junction on the Fe₂O₃ surface, (b) surface states which induced the carrier recombination onto hematite surface, and (c) high cost. For the problem (3), inactive oxide, i.e., Al₂O₃ [20], Ga₂O₃ [21], SiO_x coating [22] acted as a passivation layer for facilitating surface charge injection into the solution. Notably, amorphous metal phosphate modification films, i.e., FePi [23], CoPi [24] also improved photoactivity by suppressing the surface states. Furthermore, CoPi mainly promoted the holes transport with decrease of water oxidation kinetics [24]. These would offer an open question for discussing the origin of improved electron-hole transport on Fe₂O₃ surface by metal phosphate coating. Generally, the metal phosphates were alkaline stable relatively to inactive oxides. For example, CoPi could maintain quondam structure in contact with 1 M NaOH where only few KH₂PO₄ was added [17], while Al₂O₃ would be corroded in the same condition for long-term water splitting in high pH solutions.

* Corresponding author at: Department of Chemistry, Shantou University, Shantou 515063, P. R. China

** Corresponding authors.

E-mail addresses: lutongbu@mail.sysu.edu.cn (T. Lu), whgao@stu.edu.cn, stwhgao@163.com (W. Gao).



Scheme 1. Schematic illustration of the preparation of NiPi and its effect on surface states suppression.

Inspired by the new role of CoPi for suppressing the surface states [24], a similar effect was anticipated on NiPi. Therefore, a facile DPEC regulation method to generate thin NiPi film on Ti doped Fe_2O_3 electrode was proposed (Scheme 1). Although $\text{Fe}_2\text{O}_3/\text{NiPi}$ had been recently reported for PEC glycerol oxidation [25], but even no proof of P presence in NiPi layers was offered. To date, mechanism underlying the improvement of photoactivity by co-catalyst coating is still poorly understood. In this work, Ti doping gained lower photocurrent in low potential range compared with pristine Fe_2O_3 , which originated from low bulk charge separation and low hole injection in low potential range. Desirably, NiPi coating promoted the surface hole transport at low bias. Mott–Schottky (M–S), cyclic voltammetry (CV) measurements showed Ti doped Fe_2O_3 possessed relatively rich oxygen vacancies after high temperature annealing for improving carrier density, and NiPi coating could suppress surface states. Moreover, the catalytic property of NiPi is comparable with electrodeposited-CoPi, which had poor effect on the surface states suppression.

2. Experimental

2.1. Materials

All chemicals used in experiments were analytical grade and used as purchased from Tianjin Guangfu Fine Chemical Institute without further purification. Purified water ($18.2 \text{ M}\Omega\cdot\text{cm}$) was used for preparing all solutions. Fluorine doped tin oxide-coated glass (FTO, Zhuhai Kaivo Co., Ltd, $14 \Omega/\text{sq}$) was sequentially sonicated in soap solution, ethanol, and water. All manipulations were carried out under atmospheric conditions.

2.2. Preparation of $\alpha\text{-Fe}_2\text{O}_3$ and Ti-doped Fe_2O_3 electrodes

AKaganéite ($\beta\text{-FeOOH}$) nanorods were fabricated on FTO by modified chemical bath deposition [26] in 14 mL precursors of $\text{FeCl}_3\cdot6\text{H}_2\text{O}$ (0.15 M) and NaNO_3 (1 M) with the addition of $17.2 \mu\text{L}$ HCl (36.5–38.5%), which was added into a 20 mL Teflon-lined autoclave, a piece of FTO substrate was aslant placed with the conductive side facing the wall of the autoclave. The reaction was set at 95°C for 4 h, after cooled to room temperature, uniform FeOOH nanorod arrays were thoroughly rinsed with distilled water and dried at room temperature, followed by calcined at 750°C for 20 min in air. For Ti doped electrodes, the molar concentration ratio of K_2TiF_6 to FeCl_3 was set (0.01%, 0.05%, 0.1%), then calculated K_2TiF_6 was added to the precursor solution, the obtained electrodes were marked with 0.01%, 0.05% or 0.1% Ti: Fe_2O_3 .

2.3. Preparation of NiPi, CoPi thin film and $\text{Ni}_3(\text{PO}_4)_2$ powders

For “ NaNiPO_4 ” coating (denoted as $\text{Fe}_2\text{O}_3/\text{NaNiPO}_4$), as exhibited in Scheme 1, the NiCl_2 (0.01 M) precursor solution was drop-deposited on Fe_2O_3 surface and placed for 10 min, then the excess Ni precursor solution was rinsed with ethanol, followed by dropping neutral phosphate buffer solution (0.2 M PBS) onto the surface, and 10 min later, ethanol was used to rinse unbonded adsorbate, dried in air. The cycle was repeated once more.

For generating “NiPi” (denoted as $\text{Fe}_2\text{O}_3/\text{NiPi}$, $\text{Fe}_2\text{O}_3/\text{NaNiPO}_4$ electrode, a Pt wire, a KCl-saturated Ag/AgCl electrode were used as work electrode, counter electrode, reference electrode, respectively. All electrodes were immersed in 0.25 M Na_3PO_4 solution and then subjected to a bias of 1.23 V vs RHE under simulated sunlight for 1800 s (Fig. S2). 0.05% Ti: $\text{Fe}_2\text{O}_3/\text{NiPi}$ was also generated by employing the same method as $\text{Fe}_2\text{O}_3/\text{NiPi}$. Fig. S2 introduced a unified method, “resolvent-assisted (photo)electrochemical regulation process”.

For comparison purpose, the usually used amorphous cobalt phosphate (CoPi) was

electrodeposited onto 0.05% Ti: Fe_2O_3 according to the reported method [4,27]. (Fig. S9A)

The NiPi film was generated on FTO to obtain overpotential (η) of water oxidation at current density of $1 \text{ mA}/\text{cm}^2$. (Fig. S9C).

Nickle phosphate (taken as $\text{Ni}_3(\text{PO}_4)_2$) was synthesized according to reported method [28]. A mixed solution of 0.35 M CTAB and 0.5 M H_3PO_4 was stirred at 60°C for 1 h, then the pH was adjusted to 8.9 utilizing the dilute ammonia solution. 0.35 M $\text{Ni}(\text{NO}_3)_2$ was added into the mixed solution, forming a gel. After heating at 100°C for

24 h, the resulted solid products were filtrated, then washed, and dried at 100°C for 12 h. The final samples were obtained by centrifuging with the water and EtOH, dried at 70°C for 6 h. The obtained $\text{Ni}_3(\text{PO}_4)_2$ powders were sealed in a dry bottle. As-generated 0.05% Ti: $\text{Fe}_2\text{O}_3/\text{NiPi}$ was also sealed for FTIR microscopy study.

2.4. Characterization

The functional groups of NiPi were verified by Fourier transformation infra-red

spectrometer coupled with infra-red microscope (FTIR microscope, EQUINOX 55).

The morphology and element distribution of various electrodes was investigated on FESEM (SU8010), HRTEM (JEOL-2010 h) equipped with an EDS detector. The XRD patterns were recorded on a Bruker D8 Advance X-ray diffractometer. The absorption spectra of various electrodes were studied by the UV–vis spectrometer (Shimadzu UV-3600). The binding energies of Na, Fe, Ti, Ni, P and

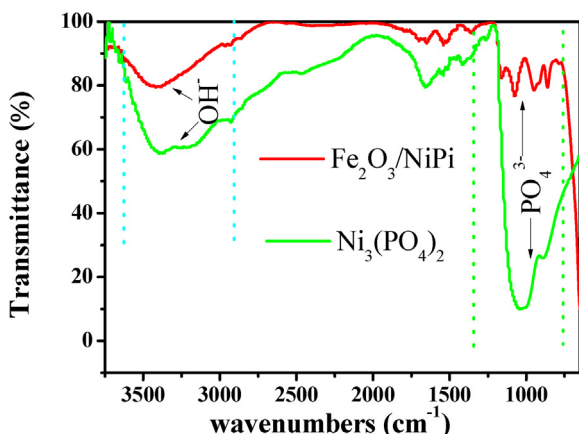


Fig. 1. FTIR microspectroscopy of 0.05% Ti:Fe₂O₃/NiPi and Ni₃(PO₄)₂.

O of 0.05% Ti:Fe₂O₃/NaNiPO₄, 0.05% Ti:Fe₂O₃/NiPi electrodes were determined by XPS (ESCALAB 250, Thermo Fisher Scientific).

2.5. (Photo)electrochemical measurements

All photoelectrochemical characterizations were performed with the CHI 660e electrochemical workstation (CHI, shanghai) in a three-electrode configuration, simulated sunlight was used for solar water oxidation measurements. The measured potential E_{Ag/AgCl} was converted to E_{RHE} according to the Nernst equation:

$$E_{RHE} = E_{Ag/AgCl} + 0.059pH + 0.197 \quad (1)$$

In the measurements of PEC regulation, 0.25 M Na₃PO₄ (pH = 12.54) was used as electrolyte, 1 M NaOH (pH = 13.6) was used in other measurements. Mott–Schottky (M–S) analysis was carried out by impedance-potential measurement in a DC potential range of 0.3–1.4 V vs RHE under dark condition.

3. Results and discussion

3.1. Structural characterization

XRD (Fig. S3), FTIR microspectroscopy (Fig. 1), SEM, TEM (Fig. 2), XPS (Fig. 3) were employed to study the composition of NiPi and morphologies.

The FTIR microspectroscopy of 0.05% Ti:Fe₂O₃/NiPi were investigated to verify the composition of NiPi (Fig. 1). The FTIR microspectroscopy for Ni₃(PO₄)₂ were also collected for comparison purpose. For Ni₃(PO₄)₂, the spectra was in agreement with the ref [28]. For 0.05% Ti:Fe₂O₃/NiPi and Ni₃(PO₄)₂, the bands in 806–1297 cm⁻¹ range were assigned to the absorption range of P–O bonds. For Ni₃(PO₄)₂, the broad bands at about 3200–3600 cm⁻¹ were attributable to the O–H stretching vibration, indicative of a large amount of hydrogen bonding [28,29]. Hydroxide was more stable, NiOOH and CoO_x were easily generated on metal phosphate LiNiPO₄ and LiCoPO₄ surface during water oxidation, the band at about 3400 cm⁻¹ for NiPi was attributable to OH⁻ bond. Other bands should be attributed to pollutant. The FTIR microspectroscopy showed NiPi was probably a nickel-hydroxyl-phosphate hybrid in nature. Broader PO₄³⁻ bands denoted that NiPi was amorphous [29], consistent with XRD results (Fig. S3).

The morphologies of Fe₂O₃, 0.05% Ti:Fe₂O₃, 0.05% Ti:Fe₂O₃/NaNiPO₄,

0.05% Ti:Fe₂O₃/NiPi were characterized by SEM and TEM. As showed in Fig. S4A, the Fe₂O₃ nanorods exhibited round and bigger due to Lorentz electromagnetic interaction force actuated by

the magnetism of Fe₂O₃, which resulted into the offset of electron beams. Both Ti doping by hydrothermal process and F⁻ assisted electro-oxidation had induced the variation of morphology of Fe₂O₃ [13], which amplified the absorption of sunlight and thus beneficial for improving photocurrent. However, Ti doping in this work showed little change of morphology (Fig. S4B), the UV absorption (Fig. S9D) also had negligible variation, because the dopant concentration was low. Inspired by the role of PO₄³⁻ for accelerating water oxidation, the NaNiPO₄ was drop-deposited on the 0.05% Ti:Fe₂O₃ surface by two cycles of sequentially dropping NiCl₂ and neutral PBS solution. Fig. 2A clearly showed a thick film coated on the 0.05%Ti:Fe₂O₃. XPS scan survey spectrum (0–1350 eV) of the 0.05% Ti:Fe₂O₃/NaNiPO₄ contained peaks corresponding to these elements Na, Ni, P, O, C (not shown here). Fig. S6B and C showed nearly no Fe 2p and Ti 2p signals was detectable in high-resolution XPS spectrum, it indicated that the XPS measurement depth was limited due to thick NaNiPO₄ film.

NiPi was generated by a newly developed DPEC regulation process. The morphology was not obvious (Fig. 2B) compared with the pristine one (Fig. S4A) in the SEM image, TEM photograph exhibited that the NiPi film was very thin (4–6 nm) (Fig. 2D). The XPS spectra of Fe 2p and Ti 2p for 0.05% Ti:Fe₂O₃/NiPi (Fig. S6B and C) showed detectable Fe 2p and Ti 2p signals, confirming few layers. No lattice fringes could be seen in the overlayer after NiPi coating, while the (104) crystal facet (Fe₂O₃, d-spacing = 0.27 nm) was observed in its crystalline core (Fig. 2E), indicating that NiPi was amorphous, in agreement with the results from XRD and FTIR microspectroscopy. EDS elemental mapping showed as generated thin NiPi film contained uniform Fe, O, Ti, Ni, P (Fig. 2C and F, Fig. S5B), further confirming phosphate species. The survey XPS spectrum also revealed the presence of Ni, P (Fig. S6A).

A detailed XPS analysis was employed to further study the bonding characteristics of both NaNiPO₄ and NiPi. The binding energies in the XPS spectra were calibrated by utilizing that of C 1s (284.8 eV). The O 1s spectrum of both NaNiPO₄ and NiPi were fitted. For NaNiPO₄, the peak at 531.1 eV was mainly attributable to PO₄³⁻ [30,31] (Fig. 3A). The another peak at 532.6 eV was attributable to absorbed H₂O, another peak at about 536.2 eV was related with Na KLL Auger emission, similar with the reported NaNiPO₄ [30]. The O 1s spectrum for NiPi was also fitted to three component peaks (Fig. 3B), the featured peak at 529.6 eV was attributable to metal–O bonds (Fe–O and Ni–O). The peak at 531 eV was attributable to surface OH⁻ and PO₄³⁻, indicative of intercalation of OH⁻, similar with surface FeOOH-modified NiPi [31]. It was further determined in Fig. S5. The peak at 532.5 eV was related with adsorbed H₂O. According to Wang et al. [32], the peak at 132.4 eV, 133.4 eV, 134.7 eV in P 2p_{3/2} spectrum was assigned to PO₄³⁻, HPO₄²⁻, H₂PO₄⁻, respectively. The P 2p_{3/2} peak of NaNiPO₄ at 133.5 eV (Fig. 3C) was attributable to HPO₄²⁻, the P 2p_{3/2} peak of NiPi fell at 132.8 eV, attributable to PO₄³⁻, positively shifted by 0.4 eV compared with the reported PO₄³⁻ [32]. Nearly no P signal corresponding to PO₄³⁻ was observable after 1800s treating in 1 M NaOH solution, indicating that PO₄³⁻ was completely deintercalated (Fig. S5). It was obvious that NaNiPO₄ underwent intercalation and deintercalation of PO₄³⁻ in 0.25 M Na₃PO₄ during the PEC regulation process. Intensity weakening of P 2p_{3/2} signal probably originated from the decrease of the detected film, in agreement with the morphology images. The Ni 2P_{3/2} and 2P_{1/2} peaks of NaNiPO₄ (Fig. 3D) fell at 856.4 eV and 874.3 eV, the high binding energy of Ni 2P_{3/2} indicated that no Ni metal and its oxide, attributable to Ni–O–P band in NaNiPO₄. The Ni 2P_{3/2} and 2P_{1/2} of NiPi fell at 855.6 eV and 873.5 eV, negatively shifted by 0.4 eV compared with recently reported NiPi (with the Ni 2P_{3/2} peak at 856 eV) [25]. The Ni 2P_{3/2} and 2P_{1/2} peaks of both NaNiPO₄ and NiPi were within the range of Ni²⁺ compounds [18,19,33a–c]. The negative shift of Ni 2P_{3/2} peak and positive shift of P 2p_{3/2} peak showed that partial electronic inter-

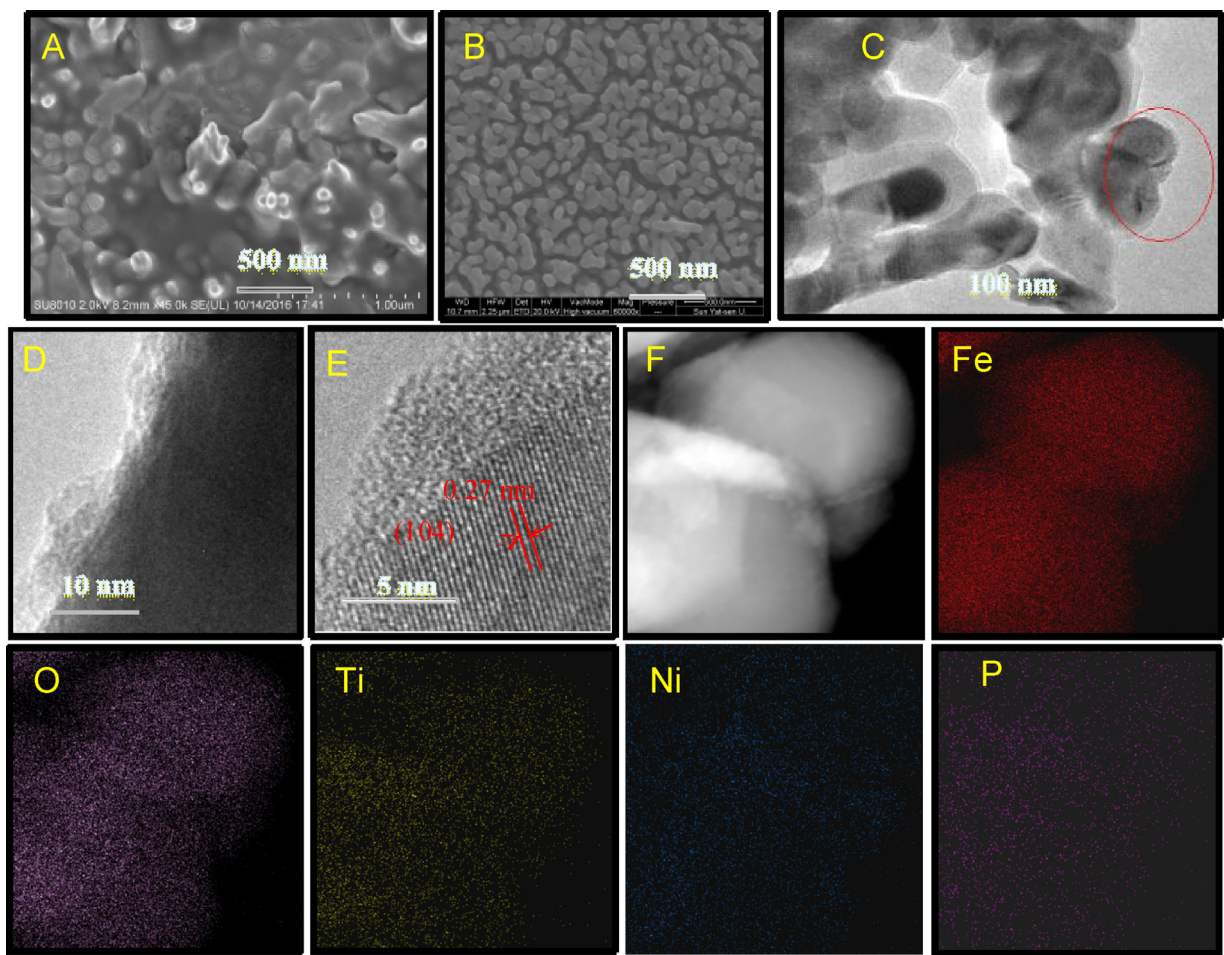


Fig. 2. SEM images of (A) 0.05% Ti:Fe₂O₃/NaNiPO₄, (B) 0.05% Ti:Fe₂O₃/NiPi, TEM images (C), (D) of 0.05% Ti:Fe₂O₃/NiPi, HRTEM photographs (E) and EDS element mapping images (F) of 0.05% Ti:Fe₂O₃/NiPi.

action of Ni-OH[−] bond and Ni-PO₄^{3−} bond. A fixed P:Ni ratio was absent, indicative of no phosphate-Ni binding in Ni-Pi, similar with the reported Co-Pi [27]. No Na KLL Auger emission and Na 1 s peak was observed (Fig. 3B and Fig. S6D) after the regulation. It was concluded that the hypothesis (Fig. S2) of self-organized composition regulation was achieved by such PEC regulation process, where Ni²⁺ was oxidized to Ni³⁺, and then Ni³⁺ oxidized water with itself reduced to Ni²⁺, accompanied with the redeposition of nickel-hydroxyl-phosphate hybrid. Although for amorphous species, its physical-chemical structure was hard to be determined, the active phosphate ions were directed to either intercalate or modify on the surface of nickel-hydroxyl-

phosphate during the new DPEC regulation process, the PO₄^{3−} existence in the interface of catalyst/solution would boost water oxidation efficiency [17]. Meanwhile, it made a relatively compact contact junction. For electrodeposition, the bulk resistance and surface energy in the different positions of the conductive substrate such as FTO was almost uniform, so that a relatively homogeneous film was probably formed. Even if the electrodeposited active film is not very homogeneous, it is enough thick (normally, < 1 ~ 2 mg/cm², 1 mg/cm² [34], 0.2 mg/cm² [35]), so that the differences are negligible. Moreover, the big overpotential at 10 mA/cm² (normally, > 100 mV) would overcome the small deficiencies, obtaining a competent electrocatalytic water oxidation property. However, the hematite film is very thin (normally, about 0.5 mg [36]), so that the co-catalyst film is limited to be thinner (normally, < 10 µg/cm², 2 µg/cm² [37], 2.7 µg/cm² [38]) for enough sunlight absorption and charge separation, the small differences of

the bulk resistance and surface energy in the different positions would be magnified, affecting the quality of thin co-catalyst film when electrodeposited [39]. The dissolution and redeposition competitively took place during the new DPEC regulation process, as a result, directing to fabricate an ultrathin and relatively homogeneous NiPi film along with the modification of active ions.

3.2. Effect of Ti doping on the PEC activity of Fe₂O₃

An optimal doped electrode (0.05% Ti:Fe₂O₃) increased the photocurrent density to 0.88 mA/cm² (Fig. S7A). Nearly no photocurrent onset potential shift was observed after various Ti doping, indicative of no variation of conduction band [14]. Nevertheless, the photocurrent of 0.05% Ti:Fe₂O₃ in low potential range was lower than pristine one. There was no observable variation in morphology and the UV absorption (Fig. S9D) after Ti doping, indicative of no capacity variation of capturing sunlight and thus no morphological variation, the variation of photocurrent should originate from other reasons. Moreover, the Ti doping didn't introduce new active species (discussed in Fig. S6E and F), but acted as the electron donors, it was usually considered as the effect of Ti doping on the bulk electronic property [10,11,13].

Impedance-potential measurements of pristine and various Ti doped Fe₂O₃ electrodes were carried out in 1 M NaOH in dark. All Mott-Schottky (M-S) curves showed positive slopes (Fig. S7B), indicating that all electrodes were *n*-type semiconductors [8,9]. With

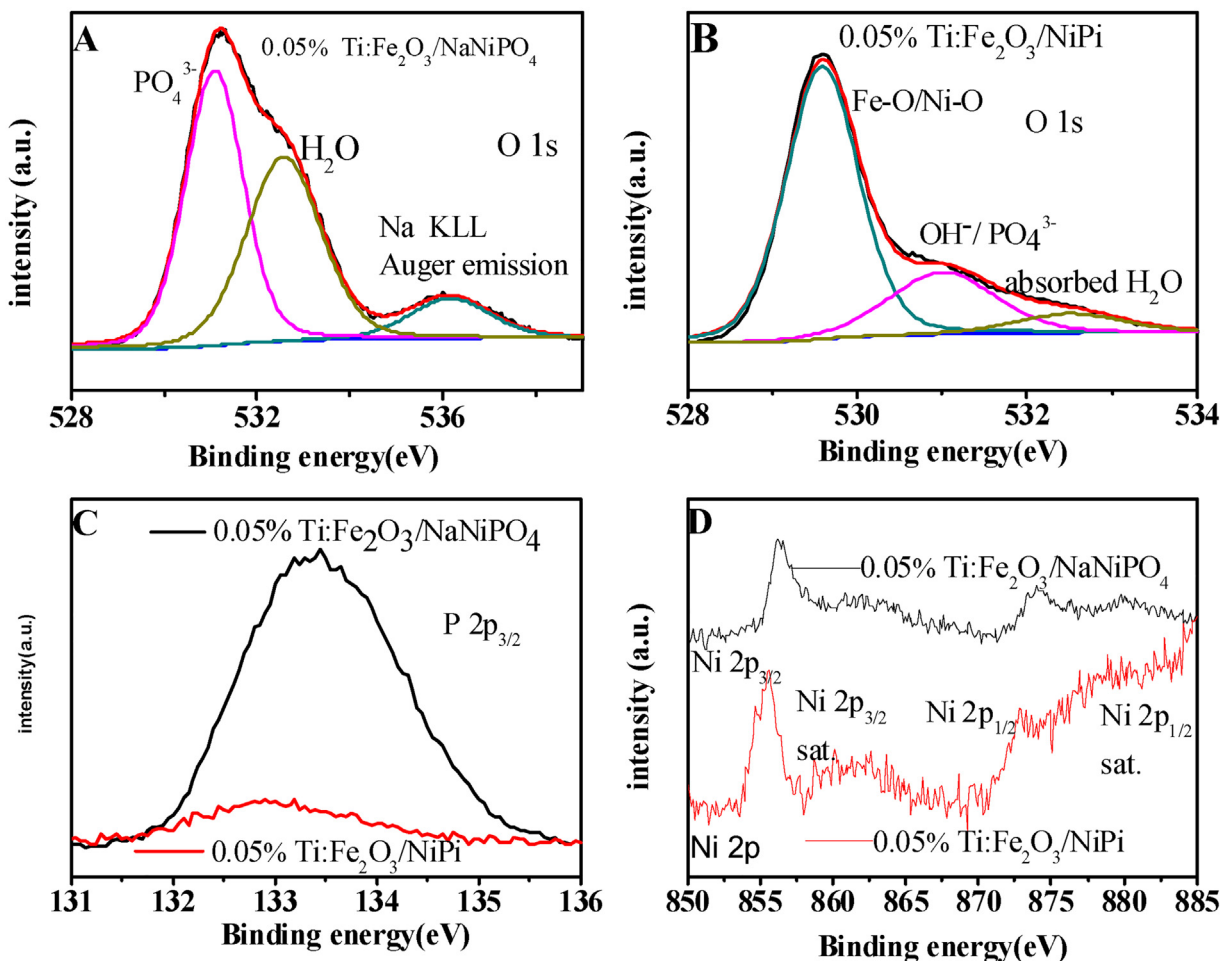


Fig. 3. High-resolution XPS spectrum of O 1s of (A) NaNiPO₄ and (B) NiPi. (C) P 2p_{3/2}, (D) Ni 2p_{3/2} spectrum of NaNiPO₄ and NiPi.

Ti doping, the slopes decreased, indicating that conductivity was improved with Ti doping [9,40]:

$$\frac{1}{C^2} = \frac{2}{\varepsilon_0 \varepsilon N_d} \left(V - V_{FB} - \frac{kT}{e} \right) \quad (2)$$

where N_d was the donor density (cm^{-3}), C is the space charge capacitance (F/cm^2), ε_0 was the vacuum permittivity ($8.854 \times 10^{-14} \text{ F}/\text{cm}$), ε was the dielectric constant of hematite ($\varepsilon = 80$ for $\alpha\text{-Fe}_2\text{O}_3$), e is the electron charge ($1.6 \times 10^{-19} \text{ C}$), V was the applied potential (V), k was the Boltzmann constant ($1.38 \times 10^{-23} \text{ J}/\text{K}$), and T was the absolute temperature ($kT/e = 0.026 \text{ V}$ at 25°C).

In Fig. S7B, N_d increased with Ti doping, N_d of 0.05% Ti doped Fe₂O₃ electrode ($4.3 \times 10^{20} \text{ cm}^{-3}$) was almost 3.3-fold increase of pristine hematite ($1.3 \times 10^{20} \text{ cm}^{-3}$), the heavy Ti doping (0.1% Ti doping in this work) hindered the charge transfer [41,42]. Enhancing Fe₂O₃ photoactivity by Ti doping was also reported as a result of the resurrection of a “dead layer” and increase of surface active sites, but the N_d remained the same as pristine Fe₂O₃ [43]. Based on the increase of N_d by Ti doping in the work, enhancing Fe₂O₃ photoactivity should be mainly attributed to enhancing bulk conductivity.

The high donor density usually improved the bulk charge separation η_{sep} .

η_{sep} was calculated based on the following equation [44,45]:

$$J_{H_2O} = J_{\max} \eta_{abs} \eta_{sep} \eta_{inj} \quad (3)$$

$$J_{H_2O_2} = J_{\max} \eta_{abs} \eta_{sep} \quad (4)$$

(where the η_{inj} was 100%, $\eta_{abs/sep/inj}$ showed the efficiency of light absorption/

charge separation/hole injection efficiency, when the H₂O₂ was oxidized, the holes on the surface were considered to completely transport into the solution, so the η_{inj} was 100%).

$$\eta_{sep} = J_{H_2O_2} / J_{\max} \eta_{abs} \quad (5)$$

The η_{sep} could give indications of the dynamic effect of Ti doping on bulk charge separation.

Higher photocurrent of 0.05% Ti:Fe₂O₃ in contact with H₂O₂ (Fig. S8) indicated higher donor density. The η_{sep} of 0.05% Ti:Fe₂O₃ was higher than Fe₂O₃ when $E > 0.72 \text{ V}$ vs RHE, but lower when $E < 0.72 \text{ V}$ vs RHE (Fig. 4B), it indicated that more free electrons recombined with holes when the force of applied bias was too low to transport them onto Pt electrode. Bulk charge separation was only improved when the potential was swept more positive, it was adverse for photoelectric conversion. The photoelectrochemical impedance spectroscopy (PEIS) by A. C. impedance

was measured to reflect the dynamic effect of Ti doping (Fig. S7C). The charge transfer resistance at the semiconductor/solution interface (R_{ct}) was usually characterized by the largest semicircle in the low-frequency range. With Ti doping, the radius decreased. The decreased R_{ct} indicated surface electron-hole pairs recombination, at least in part, was suppressed, namely, the hole injection efficiency should be improved by Ti doping, which could be estimated according to the equation [44,45]:

$$\eta_{inj} = J_{H_2O} / J_{H_2O_2} \quad (6)$$

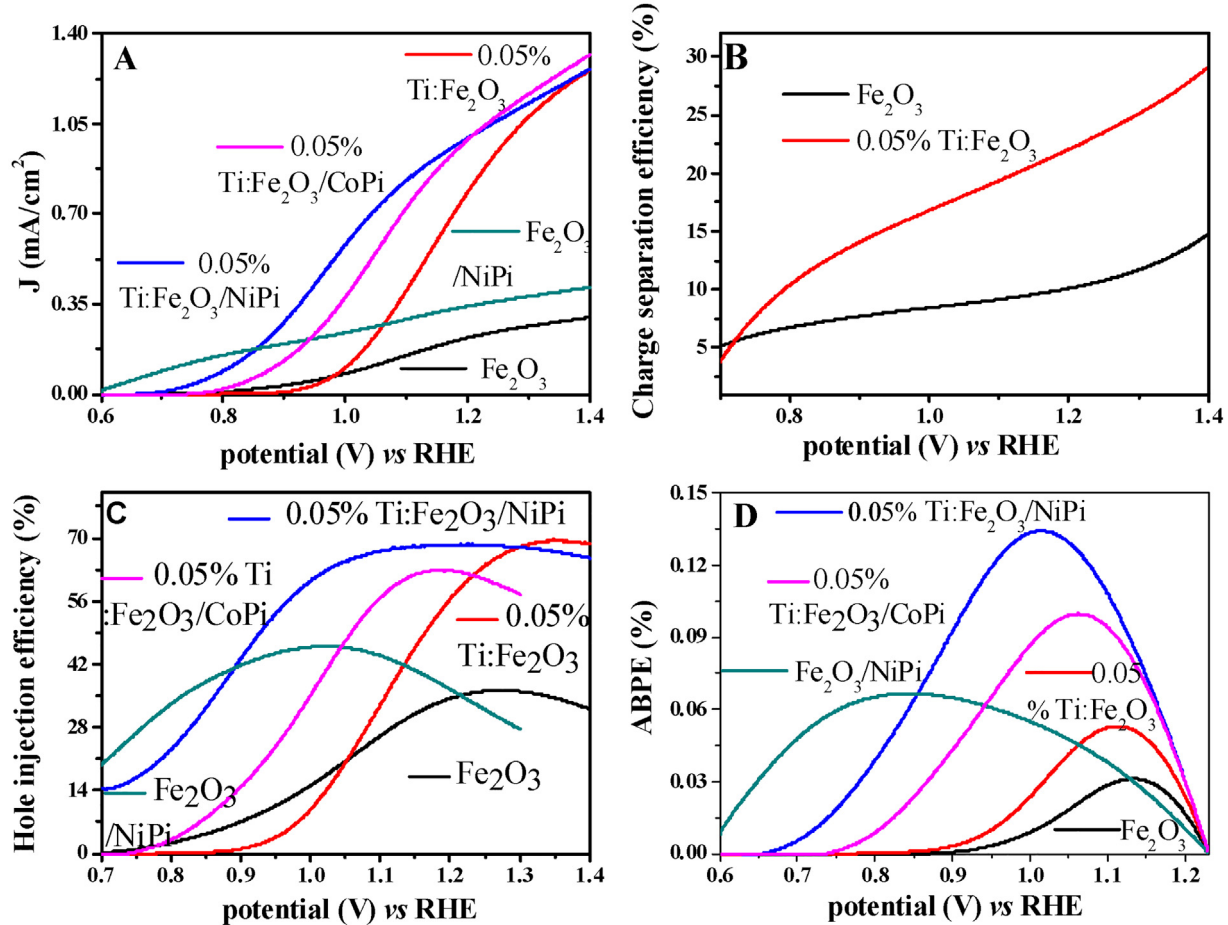


Fig. 4. (A) LSVs of Fe₂O₃, Fe₂O₃/NiPi, 0.05% Ti:Fe₂O₃, 0.05% Ti:Fe₂O₃/NiPi and 0.05% Ti:Fe₂O₃/CoPi electrodes under simulated sunlight in 1 M NaOH at a rate of 10 mV/s. (B) The bulk charge separation efficiency of pristine and 0.05% Ti doped electrodes. (C) Hole injection efficiency of Fe₂O₃, 0.05% Ti:Fe₂O₃, 0.05% Ti:Fe₂O₃/NiPi, Fe₂O₃/NiPi, and 0.05% Ti:Fe₂O₃/CoPi. (D) The ABPE of pristine Fe₂O₃, Fe₂O₃/NiPi, 0.05% Ti:Fe₂O₃, 0.05% Ti:Fe₂O₃/NiPi, and 0.05% Ti:Fe₂O₃/CoPi. It should be noted that the ABPE data should be accurately obtained in 2-electrode configuration. Here, with the comparison purpose, the ABPE data were collected from Fig. 4A in 3-electrode configuration.

The Ti doping improved hole injection efficiency in high potential range, but showed lower injection efficiency in low potential range compared with the pristine one (Fig. 4C). Previous reports revealed that the surface engineering further improved the hole injection efficiency in low potential range exhibiting a synergistical effect [46]. Herein, a newly developed co-catalyst NiPi was coupled onto the surface of the Ti doped Fe₂O₃ attempting to achieve it.

3.3. Effect of NiPi and CoPi coating on the PEC activity of Fe₂O₃

The photocurrent density of 0.05% Ti:Fe₂O₃ electrode was improved to 3.8-fold (Fig. 4A), moreover, that of 0.05% Ti:Fe₂O₃/NiPi electrode was 4.4-fold, that of single NiPi coating was 1.7-fold compared with pristine Fe₂O₃ electrode at 1.23 V vs RHE, indicative of a further increase of photocurrent by NiPi coating. All Ti doped electrodes in this work showed almost no photocurrent onset potential cathodic shift (Fig. S7A), on the contrary, pristine Fe₂O₃ electrode after NiPi coating showed an obvious onset potential cathodic shift by about 200 mV, the 0.05% Ti:Fe₂O₃/NiPi electrode showed a cathodic shift by 100 mV. It was also revealed that FTO/NiPi electrode possessed a low overpotential (η = 0.28 V) at dark current density of 1 mA/cm² (Fig. S9C). However, in light of the smaller difference of photocurrent in high potential range than in low potential range between Fe₂O₃ and Fe₂O₃/NiPi, 0.05% Ti:Fe₂O₃ and 0.05% Ti:Fe₂O₃/NiPi (Fig. 4A), it was hypothesized that the effect of NiPi coating was attributable to only improving hole injection efficiency in low potential range.

Herein, the photocurrent of Fe₂O₃/NiPi and 0.05% Ti:Fe₂O₃/NiPi electrodes in 1 M NaOH + 0.5 M H₂O₂ were plotted (Fig. S8), then the hole injection efficiency of 0.05% Ti:Fe₂O₃/NiPi and Fe₂O₃/NiPi was also plotted (Fig. 4C) to reveal the role of NiPi coating. It was observed that the hole injection efficiency of single NiPi coated electrode reached the maxima at 1.0 V vs RHE, then decreased, indicating that NiPi assisted the holes transport on 0.05% Ti:Fe₂O₃ only in low potential range, on the contrary, Ti doping only had a positive effect in high potential range.

The applied bias photon-to-current efficiency (ABPE) of pristine Fe₂O₃, 0.05% Ti:Fe₂O₃, 0.05% Ti:Fe₂O₃/NiPi, Fe₂O₃/NiPi were plotted (Fig. 4D) to reflect the surface holes transport based the equation [42]:

$$ABPE(\%) = \frac{J(1.23 - V)}{P} \quad (7)$$

where J was the photocurrent density at the measured potential V (vs RHE) under simulated light ($P = 100 \text{ mW cm}^{-2}$).

NiPi modification and Ti doping obtained $ABPE_{\max}$ at 0.85 and 1.1 V vs RHE, respectively, further confirming the cooperation of Ti doping and NiPi coating in various potential range. It was observed that the potential at $ABPE_{\max}$ of pristine Fe₂O₃ was also shifted to more cathodic direction by single NiPi coating than by Ti doping + NiPi coating, it also indicated that Ti doping hindered charge transport in low potential range, NiPi achieved it.

Improving charge transport by the cooperation of Ti doping and NiPi coating was further investigated by the OCP decay curve (Fig. 5)

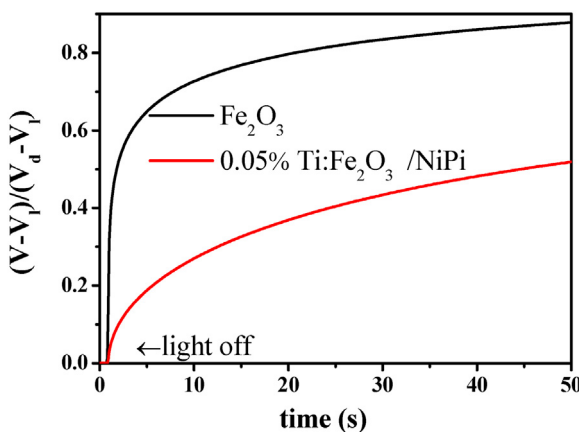


Fig. 5. The OCP decay curves of Fe_2O_3 and 0.05% $\text{Ti}:\text{Fe}_2\text{O}_3/\text{NiPi}$ while light was blocked in 1 M NaOH .

[23,47,48]. When OCP reached a stationary value (V_l) under simulated sunlight, the light was blocked, OCP gradually decayed to another stationary value (V_d), the average electron-hole recombination rate (k) was estimated based on the equation [23,47]:

$$\frac{V - V_l}{V_d - V_l} = 1 - e^{-kt} \quad (8)$$

Where the V was OCP at any time when light was blocked. The estimated average recombination rate constant of 0.05% $\text{Ti}:\text{Fe}_2\text{O}_3/\text{NiPi}$ ($k = 0.012 \text{ s}^{-1}$) was 50% of that of Fe_2O_3 ($k = 0.024 \text{ s}^{-1}$), indicating the separation of charge was improved by Ti doping and NiPi coating.

For comparison, the water and H_2O_2 oxidation properties of both 0.05% $\text{Ti}:\text{Fe}_2\text{O}_3/\text{NiPi}$ and 0.05% $\text{Ti}:\text{Fe}_2\text{O}_3/\text{CoPi}$ electrodes were carried out under illumination (Fig. 4A and Fig. S8). The 0.05% $\text{Ti}:\text{Fe}_2\text{O}_3/\text{CoPi}$ possessed higher photocurrent and lower onset potential than the pristine and Ti doped Fe_2O_3 . The effect was further enhanced by NiPi coating. Although the 0.05% $\text{Ti}:\text{Fe}_2\text{O}_3/\text{NiPi}$ had lower photocurrent when more positively swept than 0.05% $\text{Ti}:\text{Fe}_2\text{O}_3/\text{CoPi}$, the best photocurrents of a hematite anode at 1.23 V vs RHE with either element doping (2.6 mA/cm^2) [10] or a electrocatalyst (3.2 mA/cm^2) [16] or a passivation layer decorations (3.19 mA/cm^2) [22] were still far lower than the theoretical plateau value 12.6 mA/cm^2 . The surface injection efficiency of 0.05% $\text{Ti}:\text{Fe}_2\text{O}_3/\text{CoPi}$ was plotted in Fig. 4C. It was observed that the surface injection efficiency of 0.05% $\text{Ti}:\text{Fe}_2\text{O}_3/\text{NiPi}$ in less positive potential range was higher than 0.05% $\text{Ti}:\text{Fe}_2\text{O}_3/\text{CoPi}$, indicative of higher photoactivity of 0.05% $\text{Ti}:\text{Fe}_2\text{O}_3/\text{NiPi}$ in low potential range. In approaching solutions to the practical application of hematite anodes, improving the photocurrent is very important. Meanwhile, an efficient photovoltaic (PV) device in tandem with a semitransparent hematite photoanode is another important metric, which would overcome the deficiencies of low photocurrent by the integration of photoanode cells. On this point, it seems that the lower onset potential for 0.05% $\text{Ti}:\text{Fe}_2\text{O}_3/\text{NiPi}$ and higher hole injection efficiency at low bias are of more importance. Moreover, the potential at the $ABPE_{\max}$ of 0.05% $\text{Ti}:\text{Fe}_2\text{O}_3/\text{NiPi}$ shifted cathodically compared with 0.05% $\text{Ti}:\text{Fe}_2\text{O}_3/\text{CoPi}$, indicative of a higher photoactivity of the ultrathin NiPi film (Fig. 4D). The dark current of FTO/NiPi exhibited a cathodic overpotential shift by 90 mV compared with FTO/CoPi (Fig. S9B), indicating that the ultrathin NiPi film possessed better electrocatalytic water oxidation activity.

Although Ni^{3+} was reported to tend to accumulate on FeOOH modified NiPi [31] which might show adverse effect on long-term water splitting kinetics, the phenomenon was not observed in high oxidation state of Co (+3 or +4) compounds, both $\text{Ta}_3\text{N}_5/\text{Co}(\text{OH})_3$ (+3) [49] and $\text{ZnO}/[\text{Ni}^{2+}_{0.23}\text{Co}^{2+}_{0.24}\text{Co}^{3+}_{0.31}(\text{OH})_2]_{0.32}(\text{Cl})_{0.32}$ (+2

and +3) [50] photoanodes exhibited a stable photocurrent, Ni storage in minerals is higher than Co, the lower photocurrent onset potential indicated that NiPi was a potential substitute for CoPi.

3.4. Origin of improving hole injection efficiency at low bias

Previous report revealed that the improvement of photocurrent of Fe_2O_3 in contact with $[\text{Fe}(\text{CN})_6]^{3-}/4^-$ redox shuttle was estimated by $\mu\tau/D^2$ ($\mu/\tau/D$ showed the hole mobility/hole lifetime/the thickness of the electrode) [43]. Likewise, the improvement of photocurrent by Ti doping and NiPi coating in contact with 0.5 M H_2O_2 could be estimated by it. From similar SEM images (Fig. S4A and B) and similar UV-vis diffuse Spectrum absorbtion (Fig. S9D) of pristine and Ti doped Fe_2O_3 , it indicated that there was no morphological variation, pristine and Ti doped Fe_2O_3 had nearly similar thickness (D), the improvement of photocurrent should be attributed to μ or τ . In low potential range, the η_{sep} after Ti doping was lower than the pristine one in contact with H_2O_2 , indicative of lower μ in the bulk. The improvements by NiPi and CoPi coating at low bias were attributable to extending τ , which was further investigated by photocurrent dynamics developed as an approach to studying the electron-hole recombination dynamics onto the surface of Fe_2O_3 [51] and TiO_2 [52].

$$\ln D = -\frac{\tau}{t} \quad (9)$$

$$D = \frac{(I - I_f)}{(I_i - I_f)} \quad (10)$$

Where τ was the transient time constant equal to the time at $\ln D = -1$, t was the time, I was the transient photocurrent when simulated sunlight on.

The transient photocurrent was first plotted by employing a low potential (0.9 V vs RHE) photoelectrolysis along with sequential simulated sunlight off and on (Fig. 6A). When simulated sunlight on, the holes were transported onto the electrode surface due to separation of photo-generated electron-hole pairs, the initial photocurrent was generated (taken as I_i), then photocurrent decayed for three electrodes due to the electron-hole recombination at low potential, which was a process with competitive electron-hole separation and recombination. When photocurrent reached a steady value, simulated sunlight was turned off, the final photocurrent was taken as I_f . The stable photocurrent of 0.05% $\text{Ti}:\text{Fe}_2\text{O}_3/\text{NiPi}$ was highest, pristine Fe_2O_3 was higher than 0.05% $\text{Ti}:\text{Fe}_2\text{O}_3$. As anticipated, the τ (0.11 s) of 0.05% $\text{Ti}:\text{Fe}_2\text{O}_3$ almost dropped by a factor of 1.5 compared with the τ (0.16 s) of the Fe_2O_3 electrode (Fig. 6B), corresponding to the downturn of hole injection efficiency by Ti doping in low potential range. The τ (0.105 s) of the 0.05% $\text{Ti}:\text{Fe}_2\text{O}_3/\text{NiPi}$ was almost 10-fold increase of the τ (0.11 s) of 0.05% $\text{Ti}:\text{Fe}_2\text{O}_3$ (Fig. 6B) and 6.5-fold increase of the τ (0.11 s) of Fe_2O_3 , respectively. However, the τ (0.087 s) of 0.05% $\text{Ti}:\text{Fe}_2\text{O}_3/\text{CoPi}$ even dropped by a factor of 1.3 compared with the τ (0.11 s) of the 0.05% $\text{Ti}:\text{Fe}_2\text{O}_3$ electrode, and was also lower than that of pristine Fe_2O_3 , confirming that the holes on the 0.05% $\text{Ti}:\text{Fe}_2\text{O}_3/\text{CoPi}$ surface at low potential were easily recombined with the electrons. It was obviously concluded that the holes on the surface of NiPi coated electrode was more efficiently injected into electrolyte than the pristine, Ti doped, and CoPi-coated electrodes. To some extent, Ti doping hindered charge transport compared with pristine Fe_2O_3 .

3.5. Mechanistic study on the effect of Ti doping and NiPi coating on suppression of electron-hole recombination

In preceding sections, it was determined that Ti doping and NiPi coating synergistically improved surface hole transport in whole test range. Indeed, there was smaller difference of photocurrent

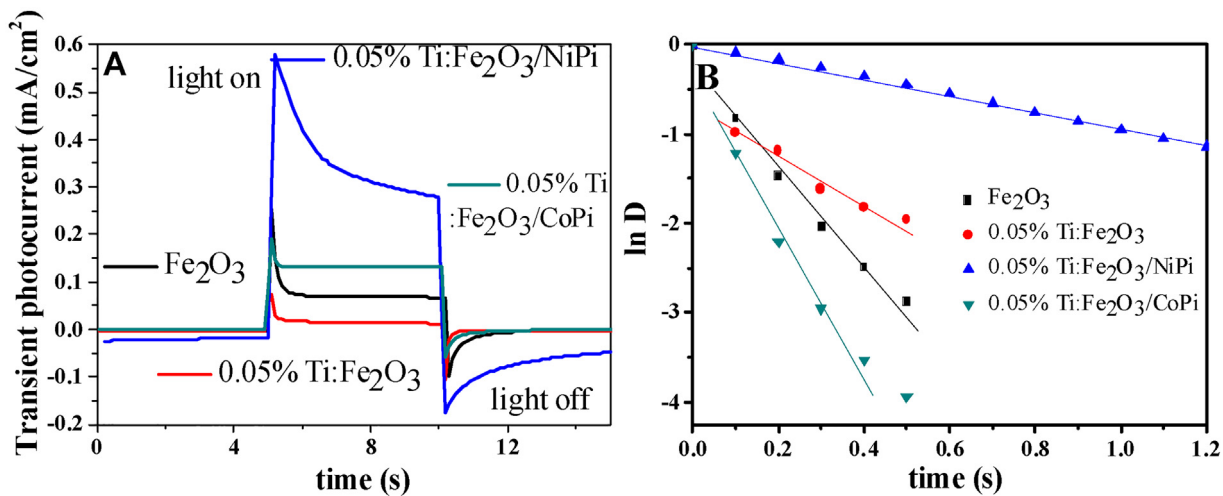


Fig. 6. (A) The transient photocurrent curves of Fe_2O_3 , 0.05% Ti:Fe₂O₃, 0.05% Ti:Fe₂O₃/NiPi, and 0.05% Ti:Fe₂O₃/CoPi at a low potential of 0.9 V vs RHE under simulated sunlight in 1 M NaOH. (B) Photocurrent dynamics curves of Fe_2O_3 , 0.05% Ti:Fe₂O₃, 0.05% Ti:Fe₂O₃/NiPi, and 0.05% Ti:Fe₂O₃/CoPi based on Fig. 6A curves.

in high potential range than in low potential range between 0.05% Ti:Fe₂O₃ and 0.05% Ti:Fe₂O₃/NiPi, Fe_2O_3 , and $\text{Fe}_2\text{O}_3/\text{NiPi}$ (Fig. 4A), similar with photocurrent trend of Al_2O_3 coated Fe_2O_3 [20], where Al_2O_3 suppressed the surface states to improve surface charge transport. The NiPi coating probably resulted into surface states suppression. To probe it, M-S, CV methods were employed.

Firstly, the M-S curves of Fe_2O_3 , 0.05% Ti:Fe₂O₃ and 0.05% Ti:Fe₂O₃/NiPi were plotted (Fig. 7A), some literatures showed that the degree of surface band bending and in turn the space charge capacitance (depletion region capacitance) would exhibited little change in surface states (oxygen vacancies) region [23,53]. The curve slope of pristine Fe_2O_3 was unchanged initially, then decreased between 1 V and 1.2 V vs RHE ("showing no obvious curvature"), indicating that surface states region of Fe_2O_3 fell in the range of 1–1.2 V vs RHE [23,54]. In oxygen vacancies, the electron-hole pairs recombined, namely, cycles of reduction from Fe^{3+} to Fe^{2+} due to electron and then oxidation from Fe^{2+} to Fe^{3+} due to hole, holes couldn't be used for effective water oxidation (Scheme 1), which accounted for the high photocurrent onset potential. The slopes of 0.05% Ti:Fe₂O₃, 0.05% Ti:Fe₂O₃/NiPi and 0.05% Ti:Fe₂O₃/CoPi were almost unchanged ("showing a curvature") in whole potential range, which might be considered as a result of the suppression of surface states [23,53]. However, rich oxygen vacancies could improve donor density [55]. As a result, it could lower the slope of M-S curve, so it might appear as if it had a curvature. Suppression of the surface states should be further verified. The variation of oxygen vacancies density was one of evaluation methods [21,23,56].

Secondly, the surface states suppression was directly tested by cyclic voltammetry

(CV) to prove the effect of Ti doping on surface states suppression (Fig. 7B and C) [23,57,58]. The reduction peak of pristine Fe_2O_3 and 0.05% Ti:Fe₂O₃ fell at about 1.17 V vs RHE, indicative of reduction from Fe^{3+} to Fe^{2+} . The position of reduction peak was in agreement with the verified surface states region (1–1.2 V vs RHE) (Fig. 7A). It confirmed that oxygen vacancies existed on the surface of both Fe_2O_3 and 0.05% Ti:Fe₂O₃. The area of reduction peak of 0.05% Ti:Fe₂O₃ exceeded the pristine one, indicating that the density of oxygen vacancies on pristine Fe_2O_3 surface was low, it induced adverse effect of surface states. Ti doped Fe_2O_3 after high temperature annealing possessed relatively rich oxygen vacancies. It excluded the positive effect of Ti doping on suppression of surface states. Based on obvious improvement of N_d , the improvement of

photoactivity by Ti doping was attributable to improving conductivity.

No reduction peak (Fig. 7D) existed in the verified surface states region for 0.05% Ti:Fe₂O₃/NiPi, while the reduction peak of 0.05% Ti:Fe₂O₃/CoPi was observable (Fig. 7E), confirming the suppression of surface states by NiPi coating rather than CoPi coating. Thus, holes were easily injected into the solution from NiPi film for effective water oxidation (Scheme 1).

Surface states was a great limitation for improving photoactivity of Fe_2O_3 , the benchmark IrO_2 -modified cauliflower-type Fe_2O_3 nanostructure electrode was also limited by it [16]. Recent studies were focused on it, the NiOOH [39] and CoPi [24] which were considered as best electrocatalysts, were also employed to suppress the surface states. In this work, the photocurrent of 0.05% Ti:Fe₂O₃ after NiPi coating was almost unchanged in high potential range (Fig. 4A), indicative of poor OER kinetics, and no reduction peak (Fig. 7D) of Fe and Ni also indicated that the Ni-based film was ultrathin. Balancing the slower recombination against the slower water oxidation kinetics will be further taken into consideration in our lab.

In addition, water splitting in neutral seawater (pH 7–8) was an ideal way for producing solar fuel, however, photocurrent performance of Fe_2O_3 was poor in neutral electrolyte. In light of the fact that seawater contained PO_4^{3-} (order of magnitude: $\mu\text{mol/L}$), glucose and methanol was added into neutral PBS attempting to amplify hole transport when simulating long-term photolysis. Preliminary results showed that low concentration of glucose couldn't be oxidized due to the suppression effect of PO_4^{3-} adsorbed $\text{Fe}_2\text{O}_3/\text{NiPi}$, and methanol was probably an effective scavenger (Fig. S10).

4. Conclusions

In this work, an effective co-catalyst NiPi was generated by a new DPEC regulation process, similar with self-organized fabrication of TiO_2 nanotubes, which was used to improve photocurrent and hole injection efficiency of Ti doped Fe_2O_3 electrode in low potential range. Photocurrent dynamics study exhibited that electron-hole recombination by NiPi coating decreased compared with Ti doping at a low potential. Mechanistic study by M-S, CV methods further revealed that the suppression of surface states by NiPi coating was accountable for improving photoactivity at low bias. Ti doped Fe_2O_3 possessed relatively rich oxygen vacancies after high temperature annealing, improving the conductivity

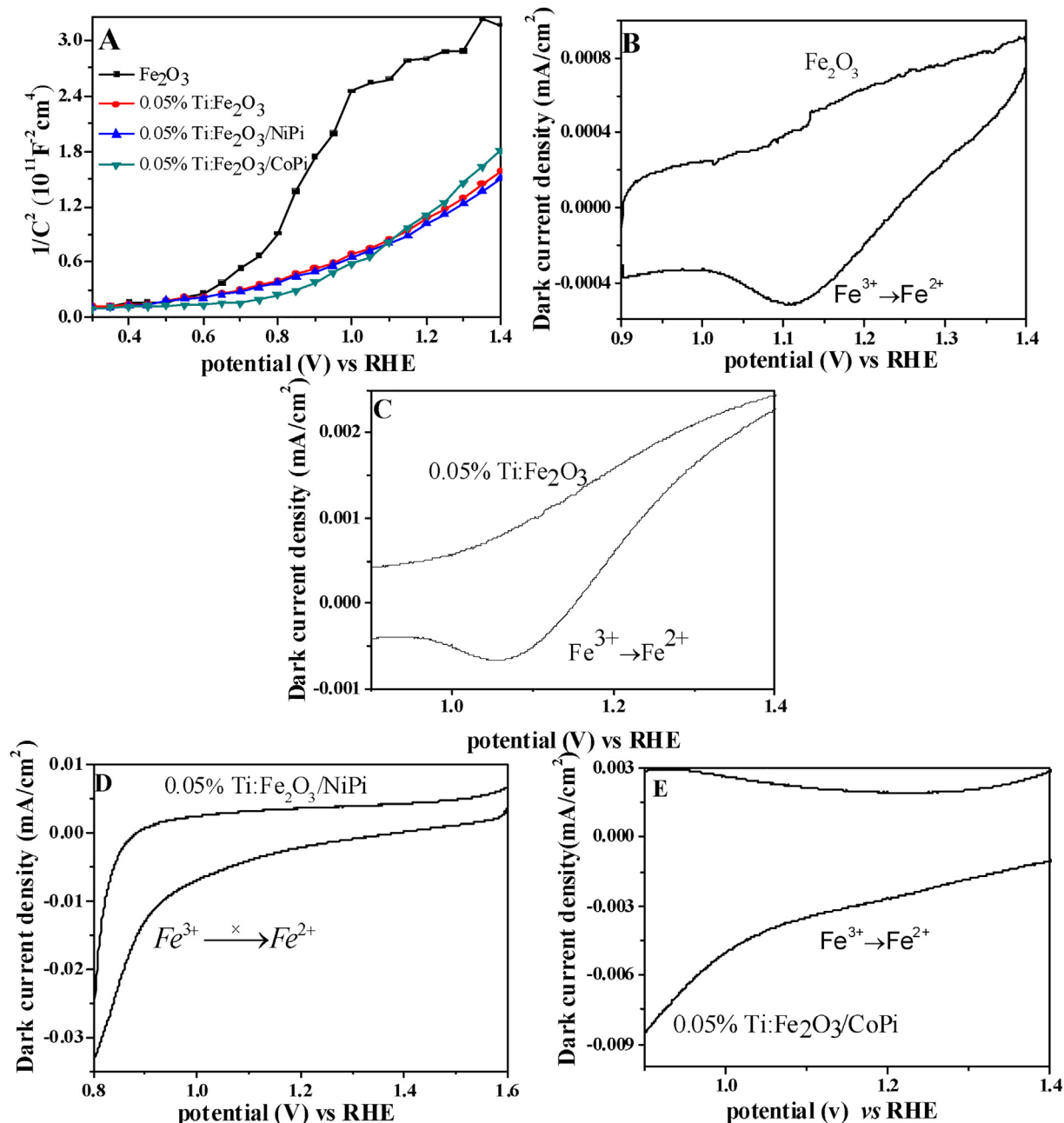


Fig. 7. Investigation of surface states suppression. (A) The M-S measurements of Fe_2O_3 , 0.05% Ti: Fe_2O_3 , 0.05% Ti: $\text{Fe}_2\text{O}_3/\text{NiPi}$, and 0.05% Ti: $\text{Fe}_2\text{O}_3/\text{CoPi}$. CV measurements of (B) Fe_2O_3 , (C) 0.05% Ti: Fe_2O_3 , (D) 0.05% Ti: $\text{Fe}_2\text{O}_3/\text{NiPi}$ (E) 0.05% Ti: $\text{Fe}_2\text{O}_3/\text{CoPi}$ in 1 M NaOH in dark.

and photoactivity at high bias. CoPi coating couldn't suppress the surface states.

Appendix A. Supplementary data

Supplementary data associated with this article can be found, in the online version, at <http://dx.doi.org/10.1016/j.apcatb.2017.06.042>.

Acknowledgements

We are grateful for the financial support from the Natural Science Foundation of Guangdong Province (No. 2014A030313480), the Science & Technology Project of Guangdong Province (No. 2013B030600001 & No. 2016A020223014) and the National Natural Science Foundation of China (No. 51272152/E0208), and also grateful for Sun Yat-Sen University for kinds of structural characterizations.

References

- [1] Y.j. Lin, G.B. Yuan, S. Sheehan, S. Zhou, D.W. Wang, *Energy Environ. Sci.* 4 (2011) 4862–4869.
- [2] D.K. Zhong, M. Cornuz, K. Sivula, M. Gratzel, D.R. Gamelin, *Energy Environ. Sci.* 4 (2011) 1759–1764.
- [3] G.M. Carroll, D.K. Zhong, D.R. Gamelin, *Energy Environ. Sci.* 8 (2015) 577–584.
- [4] D.K. Zhong, D.R. Gamelin, *J. Am. Chem. Soc.* 132 (2010) 4202–4207.
- [5] D.K. Zhong, J.W. Sun, H. Inumaru, D.R. Gamelin, *J. Am. Chem. Soc.* 131 (2009) 6086–6087.

[6] N.J. Cherepy, D.B. Liston, J.A. Lovejoy, H.M. Deng, J.Z. Zhang, *J. Phys. Chem. B.* 102 (1998) 770–776.

[7] O. Khaselev, J.A. Turner, *Science* 280 (1998) 425–427.

[8] J.H. Kennedy, K.W. Frese, *J. Electrochem. Soc.* 125 (1978) 709–714.

[9] M.P. Dare-Edwards, J.B. Goodenough, A. Hamnett, P.R. Trevellick, *J. Chem. Soc. Faraday Trans.* 79 (1983) 2027–2041.

[10] G.M. Wang, Y.C. Ling, D.A. Wheeler, K.E.N. George, K. Horsley, C. Heske, J.Z. Zhang, Y. Li, *Nano Lett.* 11 (2011) 3503–3509.

[11] D.W. Kim, S.C. Riha, E.J. DeMarco, A.B.F. Martinson, O.K. Farha, J.T. Hupp, *ACS Nano* 12 (2014) 12199–12207.

[12] R. Franking, L. Li, M.A. Lukowski, F. Meng, Y.Z. Tan, R.J. Hamers, S. Jin, *Energy Environ. Sci.* 6 (2013) 500–512.

[13] A.W. Pu, J.J. Deng, M. Li, J. Gao, H. Zhang, Y.Y. Hao, J. Zhong, X.H. Sun, *J. Mater. Chem. C* 2 (2014) 2491–2497 (A).

[14] C.H. Miao, S.L. Ji, G.P. Xu, G.D. Liu, L.D. Zhang, C.H. Ye, *A.C.S. Appl. Mater. Interfaces* 4 (2012) 4428–4433.

[15] M. Marelli, A. Naldoni, A. Minguzzi, M. Allieta, T. Virgili, G. Scavia, S. Recchia, R. Psaro, V. Dal Santo, *A.C.S. Appl. Mater. Interfaces* 6 (2014) 11997–12004.

[16] S.D. Tilley, M. Cornuz, K. Sivula, M. Gratzel, *Angew. Chem. Int. Ed.* 49 (2010) 6405–6408.

[17] K.J. Mcdonald, K. Choi, *Chem. Mater.* 23 (2011) 1686–1693.

[18] G.M. Wang, Y.C. Ling, X.H. Lu, T. Zhai, F. Qian, Y.X. Tong, Y. Li, *Nanoscale* 5 (2013) 4129–4133.

[19] A.G. Tamirat, W.N. Su, A.A. Dubale, H.M. Chen, B.J. Hwang, *J. Mater. Chem. A* 3 (2015) 5949–5961.

[20] F.L. Formal, N.T. etreault, M. Cornuz, T. Moehl, M. Gratzel, K. Sivula, *Chem. Sci.* 2 (2011) 737–743.

[21] L. Steier, I. Herraiz-Cardona, S. Gimenez, F. Fabregat-Santiago, J. Bisquert, S.D. Tilley, M. Gratzel, *Adv. Funct. Mater.* 24 (2014) 7681–7688.

[22] H.J. Ahn, K.Y. Yoon, M.J. Kwak, J.H. Jang, *Angew. Chem. Int. Ed.* 55 (2016) 9922–9926.

[23] Z.F. Hu, Z.R. Shen, J.C. Yu, *Chem. Mater.* 28 (2016) 564–572.

[24] G.M. Carroll, D.R. Gamelin, *J. Mater. Chem. A* 4 (2016) 2986–2994.

[25] R.F. Chong, B.Y. Wang, D.L. Li, Z.X. Chang, L. Zhang, *Solar Energy Materials & Solar Cells*. 160 (2017) 287–293.

[26] Y.C. Ling, G.M. Wang, D.A. Wheeler, J.Z. Zhang, Y. Li, *Nano Lett.* 11 (2011) 2119–2125.

[27] M.W. Kanan, J. Yano, Y. Surendranath, M. Dincă, V.K. Yachandra, D.G. Nocera, *J. Am. Chem. Soc.* 132 (2010) 13692–13701.

[28] J. Yu, A. Wang, J. Tan, X. Li, J.A. Van Bokhoven, Y. Hu, *J. Mater. Chem.* 18 (2008) 3601–3607.

[29] Y.Y. Tong, C.D. Gu, J.L. Zhang, M.L. Huang, H. Tang, X.L. Wang, J.P. Tua, *J. Mater. Chem. A* 3 (2015) 4669–4678.

[30] M. Minakshi, D. Mitchell, R. Jones, F. Alenazey, T. Watcharatharapong, S. Chakraborty, R. Ahujaf, *Nanoscale* 8 (2016) 11291–11305.

[31] Y.B. Li, C. Zhao, *Chem. Mater.* 28 (2016) 5659–5666.

[32] Q. Wang, L. Zhong, J. Sun, J. Shen, *Chem. Mater.* 17 (2005) 3563–3569.

[33] (a) A.N. Mansour, *Surf. Sci. Spectra* 3 (1994) 239–246;
(b) A.N. Mansour, C.A. Melendres, *Surf. Sci. Spectra* 3 (1994) 247–254;
(c) A.N. Mansour, C.A. Melendres, *Surf. Sci. Spectra* 3 (1994) 255–262.

[34] G. Zhang, G.C. Wang, Y. Liu, H.J. Liu, J.H. Qu, J.H. Li, *J. Am. Chem. Soc.* 138 (2016) 14686–14693.

[35] D. Li, H. Baydoun, C.N. Verani, S.L. Brock, *J. Am. Chem. Soc.* 138 (2016) 4006–4009.

[36] Y.C. Zhang, Z.C. Zhou, C.C. Chen, Y.K. Che, H.W. Ji, W.H. Ma, J. Zhang, D.Y. Song, J.C. Zhao, *A.C.S. Appl. Mater. Interfaces* 6 (2014) 12844–12851.

[37] C.G. Morales-Guio, M.T. Mayer, A. Yella, S.D. Tilley, M. Gratzel, X.L. Hu, *J. Am. Chem. Soc.* 137 (2015) 9927–9936.

[38] J.W. Huang, G.W. Hu, Y. Ding, M.C. Pang, B.C. Ma, *J. Catal.* 340 (2016) 261–269.

[39] F. Malaria, A. Minguzzi, M. Marelli, S. Morandi, R. Psaro, V.Dal. Santo, A. Naldoni, *ACS Catal.* 5 (2015) 5292–5300.

[40] R.V.D. Krol, M. Grätzel, Springer, New York, 2012.

[41] C.H. Miao, T.F. Shi, G.P. Xu, S.L. Ji, C.H. Ye, *A.C.S. Appl. Mater. Interfaces* 5 (2013) 1310–1316.

[42] Y.F. Yuan, J.W. Gu, K.H. Ye, Z.S. Chai, X. Yu, X.B. Chen, C.X. Zhao, Y.M. Zhang, W.J. Mai, *ACS Appl. Mater. Interfaces* 8 (2016) 16071–16077.

[43] O. Zandi, B.M. Klahr, T.W. Hamann, *Energy Environ. Sci.* 6 (2013) 634–642.

[44] H. Dotan, K. Sivula, M. Gratzel, A. Rothschild, S. Warren, *Energy Environ. Sci.* 4 (2011) 958–964.

[45] Y. Yang, M. Forster, Y.C. Ling, G.M. Wang, T. Zhai, Y.T. Tong, A.J. Cowan, Y. Li, *Angew. Chem. Int. Ed.* 128 (2016) 3464–3468.

[46] A.J. Abel, A.M. Patel, S.Y. Smolin, B. Opasanont, J.B. Baxter, *J. Mater. Chem. A* 4 (2016) 6495–6504.

[47] J. Kim, D. Monllor-Satoca, W. Choi, *Energy Environ. Sci.* 5 (2012) 7647–7656.

[48] D. Monllor-Satoca, R. Gomez, W. Choi, *Environ. Sci. Technol.* 46 (2012) 5519–5527.

[49] M. Li, W. Luo, D. Cao, X. Zhao, Z. Li, T. Yu, Z. Zou, *Angew. Chem. Int. Ed.* 52 (2013) 11016–11020.

[50] M.F. Shao, F.Y. Ning, M. Wei, D.G. Evans, X. Duan, *Adv. Funct. Mater.* 24 (2014) 580–586.

[51] X.J. Shi, K. Zhang, J.H. Park, *Int. J. Hydrogen Energy* 38 (2013) 12725–12732.

[52] C.J. Lin, Y.T. Lu, C.H. Hsieh, S.H. Chien, *Appl. Phys. Lett.* 94 (2009) 113102.

[53] R. Franking, L.S. Li, M.A. Lukowski, F. Meng, Y.Z. Tan, R.J. Hamers, S. Jin, *Energy Environ. Sci.* 6 (2013) 500–512.

[54] G. Liu, J. Shi, F. Zhang, Z. Chen, J. Han, C. Ding, S. Chen, Z. Wang, H. Han, C. Li, *Angew. Chem. Int. Ed.* 53 (2014) 7295–7299.

[55] Y.C. Ling, G.M. Wang, H.Y. Wang, Y. Yang, Y. Li, *ChemSusChem* 7 (2014) 848–853.

[56] L. Steier, I. Herraiz-Cardona, S. Gimenez, F. Fabregat-Santiago, J. Bisquert, S.D. Tilley, M. Grätzel, *Adv. Funct. Mater.* 24 (2014) 7681–7688.

[57] J. Moir, N. Soheilinia, P. O'Brien, A. Jelle, C.M. Grozea, D. Faulkner, M.G. Helander, G.A. Ozin, *ACS Nano* 7 (2013) 4261–4274.

[58] D. Wodka, R.P. Socha, E. Bielanska, M. Elzbieciak-Wodka, P. Nowak, P. Warszynski, *Appl. Surf. Sci.* 319 (2014) 173–180.